

LONG WAVELENGTH ASTROPHYSICS

by

Liam Dean Connor

A thesis submitted in conformity with the requirements
for the degree of Doctor of Philosophy
Graduate Department of Astronomy and Astrophysics
University of Toronto

© Copyright 2016 by Liam Dean Connor

Abstract

Long wavelength astrophysics

Liam Dean Connor

Doctor of Philosophy

Graduate Department of Astronomy and Astrophysics

University of Toronto

2016

To Pop and my infinitely supportive parents

Acknowledgements

Contents

1	Non-cosmological but Extragalactic Fast Radio Bursts	1
1.1	Chapter Overview	1
1.2	Introduction	1
1.3	Introduction	1
1.4	Supernova Remnants	2
1.4.1	Event Rates	4
1.4.2	Young SNR Pulsars	6
1.5	Predictions	6
1.6	Conclusions	11
1.7	Acknowledgements	11
	Bibliography	12

List of Tables

- 1.1 This table summarizes a number of FRB models by classifying them as cosmological, extragalactic but non-cosmological, Galactic, and terrestrial. The seven columns are potential observables of FRBs and each row gives their consequence for a given model (Blitzars (Falcke & Rezzolla, 2014), compact object mergers (Mickaliger et al., 2012; Totani, 2013), exploding primordial blackholes (Barrau et al., 2014), bursts from magnetars (Lyubarsky, 2014), edge-on disk galaxies (Xu & Han, 2015), circumnuclear magnetars (Pen & Connor, 2015), supernova remnant pulsars, stellar flares (Loeb et al., 2014), and terrestrial RFI (Hippke et al., 2015).). For the latter, we subdivide the RFI into planar RFI (2D) coming from the earth’s surface, and 3D RFI coming from objects like satellites. Since scintillation only affects unresolved images, cosmological sources that are not scattered near the source will not scintillate in our Galaxy, while non-cosmological sources whose screens are intrinsic will. For Faraday rotation and scintillation we assume the RM and SM comes from the same place as the DM, e.g. the IGM for cosmological sources, though such models could introduce a more local Faraday effect or a scattering screen. Even though all models have to explain the observed $375\text{-}1600\text{ pc cm}^{-3}$, some models predict a wider range of DM. For instance, in the circumnuclear magnetar or edge-on disk disk scenarios there ought to be bursts at relatively low DM that simply have not been identified as FRBs. In our supernova remnant model DMs should be very large early in the pulsar’s life, though this window is short and therefore such high DM bursts would be rare. .

7

Chapter 1

Beamforming

1.1 Chapter Overview

In an era when electric fields can be sampled billions of times per second, radio telescopes are becoming more and more digital. While the cost of constructing large single-dish telescopes is not expected to decrease substantially, the cost of building large computing clusters is, which makes it economically and strategically sensible to point one's telescope in software, as with digital beamforming. Beamforming is particularly essential to CHIME. The pulsar back-end will rely on brute-force beamforming in order to track ten sources at a time, 24-7. The FRB experiment will FFT-beamform to generate 1024 fan-beams, in order to search them in real time for radio transients. And the cosmology experiment has always left itself the option of beamforming, whose computing cost scales as $N \log N$, as an alternative to the full N^2 correlation. This chapter outlines the basic theory behind digital beamforming, and describes the commissioning of the first beamformer on CHIME Pathfinder. This includes the synthesis of several different software packages, the implementation of an early scheduler, and an automated point-source calibration daemon that removes drifting instrumental gains in real-time. We will also detail early pulsar work and the creation of an ongoing VLBI FRB search between the DRAO and ARO. The latter will include constraints on α .

1.2 Introduction

1.3 Theory and Implementation

Beamforming is a signal processing technique that allows for spatial filtering, and has greatly benefited a diverse set of fields from radar and wireless communications to radio astronomy. Historically, this was

By coherently combining the voltages of a multi-element array, sensitivity can be allocated to small regions of the sky and the array's effective forward gain can be increased. The signal from each antenna, x_n , is multiplied by a complex weight whose phases, ϕ_n , are chosen to destructively interfere radio waves in all directions but the desired pointing. The signals from all antennas are then combined to give the formed-beam voltage stream, X_{BF} .

$$X_{\text{BF}} = \sum_{n=1}^N a_n e^{i\phi_n} x_n \quad (1.1)$$

Here a_n are real numbers that can be used to as amplitude weightings for the antennas. If we define a more general complex weighting, $w_n \equiv a_n e^{i\phi_n}$, and switch to vector notation, Eq. ?? becomes,

$$X_{\text{BF}} = \mathbf{w} \mathbf{x}^T. \quad (1.2)$$

In general, X_{BF} and \mathbf{x}^T will be functions of time and frequency. This is also true for \mathbf{w} , unless one needs a static, non-tracking beam – which is the case for the CHIME Pathfinder's transient search. We can write this explicitly as follows.

$$\mathbf{w}_{t\nu} = (a_1(\nu)e^{i\phi_1(\nu)}, a_2(\nu)e^{i\phi_2(\nu)}, \dots, a_N(\nu)e^{i\phi_N(\nu)}) \quad (1.3)$$

$$\mathbf{x}_{t\nu} = (x_1(t, \nu), x_2(t, \nu), \dots, x_N(t, \nu)) \quad (1.4)$$

The voltage stream is then effectively squared and integrated to give a visibility stream. In the case of CHIME, X_{BF} corresponds to a single polarization so to get the full Stokes information one must compute the north-south polarization's autocorrelation, the east-west autocorrelation, and their cross-correlation. The Stokes vector can be written as,

$$\begin{pmatrix} I \\ Q \\ U \\ V \end{pmatrix} = \begin{pmatrix} X_{\text{ew}}X_{\text{ew}}^* + X_{\text{ns}}X_{\text{ns}}^* \\ X_{\text{ew}}X_{\text{ew}}^* - X_{\text{ns}}X_{\text{ns}}^* \\ \Re(X_{\text{ew}}X_{\text{ns}}^*) \\ \Im(X_{\text{ew}}X_{\text{ns}}^*) \end{pmatrix}. \quad (1.5)$$

1.3.1 Geometric phase

We now need to calculate ϕ_n across the array. Ignoring instrumental phases for now, one can compute the geometric phases for an antenna by projecting its position vector, \mathbf{d}_n , onto the pointing vector, $\hat{\mathbf{k}}$. This gives,

$$\phi_n = \frac{2\pi}{\lambda} \mathbf{d}_n \cdot \hat{\mathbf{k}} \quad (1.6)$$

where we have taken \mathbf{d}_n to be the baseline vector between feed n and an arbitrary reference point, and ϕ_n is the corresponding phase difference. A sketch for this is shown in Fig. ?? on page ??.

To calculate the projection $\mathbf{d}_n \cdot \hat{\mathbf{k}}$, we need to go from celestial coordinates, in this case equatorial, to geographic coordinates. This requires only a source location, an observer location, and an observing time. For the latter we use local sidereal time (LST), which is the *RA* of the local meridian. This can be determined by an observer's longitude and a time, e.g. a Coordinated Universal Time (UTC). A source's hour angle is simply the difference between *LST* and its *RA*,

$$HA = LST - RA. \quad (1.7)$$

We use the standard interferometric (u, v, w) coordinate system to describe our baseline vector, \mathbf{d}_n . This is a right-handed coordinate system where u (east-west) and v (north-south) are in the plane whose normal is the zenith, and w measures the vertical direction (Thompson et al., 1986). They are defined in numbers of wavelengths, with $u = d_{\text{ew}}/\lambda$, $v = d_{\text{ns}}/\lambda$, and $w = d_{\text{vert}}/\lambda$. Eq. ?? can be expanded as,

$$\phi_n = 2\pi (u, v, w) \cdot \hat{\mathbf{k}} \quad (1.8)$$

$$= 2\pi \left(u \hat{\mathbf{u}} \cdot \hat{\mathbf{k}} + v \hat{\mathbf{v}} \cdot \hat{\mathbf{k}} + w \hat{\mathbf{w}} \cdot \hat{\mathbf{k}} \right), \quad (1.9)$$

where each projection component can be obtained using spherical trigonometry. Though we do not go through the derivation here, it is given by the following product,

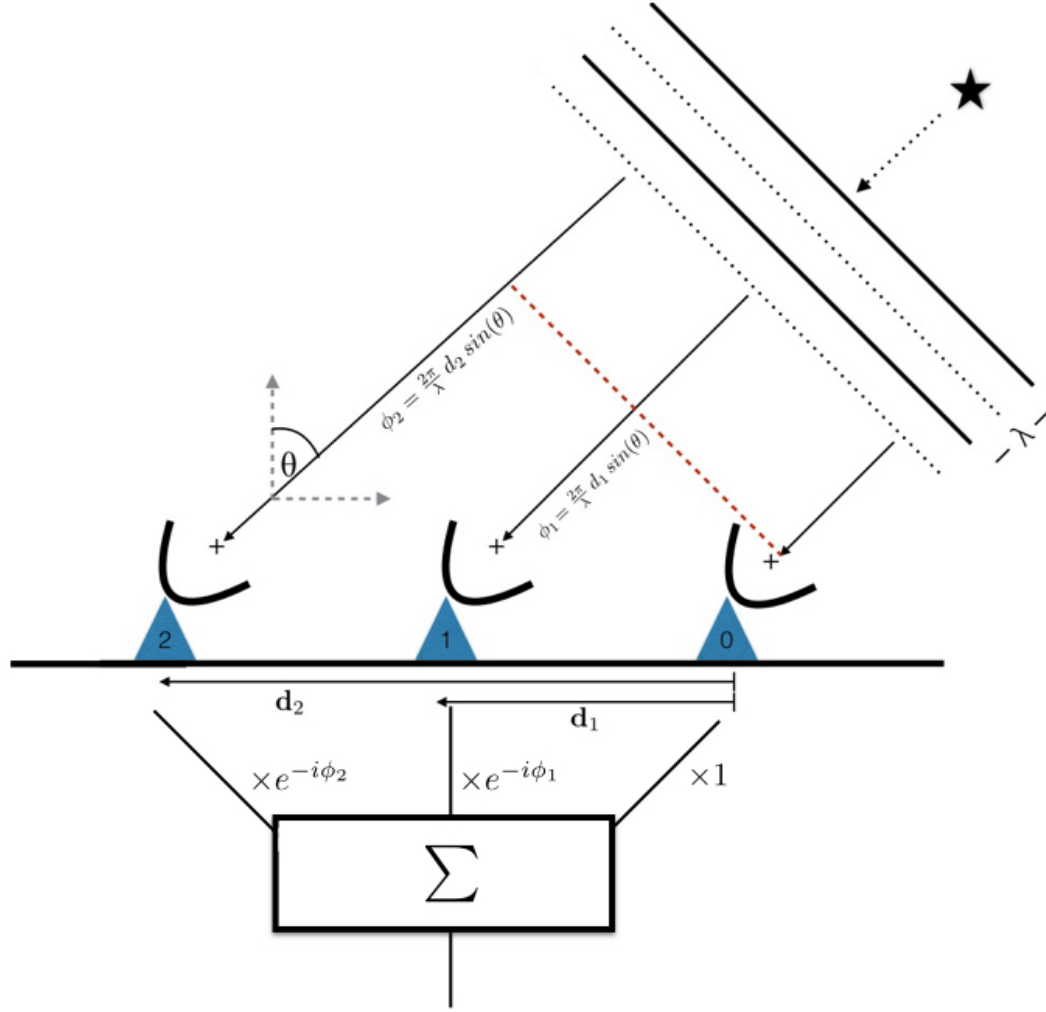


Figure 1.1: Diagrammatic example of a three-element beamformer. The wavefront from a far-field point-source arrives at each antenna at different times, but the delay is calculable given an array configuration and a direction to the object. Complex weights can be applied to each antenna's voltage time-stream to account for the geometric delay, allowing for the signals to be summed coherently.

$$\mathbf{d}_n \cdot \hat{\mathbf{k}} = \lambda \begin{pmatrix} u, & v, & w \end{pmatrix} \cdot \begin{pmatrix} -\cos\delta \sin H A \\ \cos(lat) \sin\delta - \sin(lat) \cos\delta \cos H A \\ \sin(lat) \sin\delta + \cos(lat) \cos\delta \cos H A \end{pmatrix}. \quad (1.10)$$

These phases are not only essential to beamforming but also for the fringestopping process, which is ubiquitous in interferometric analysis and is described in Sec. ??.

Variable	Coordinate
δ	Source declination
RA	Source right ascension
LST	Local sidereal time
HA	Source hour angle
alt	Source altitude
az	Source azimuth
lat	Telescope latitude
lon	Telescope longitude

1.4 Pathfinder beamformer

1.4.1 Instrumental phases

In a real experiment, if the voltages from each antenna, x_n , are summed without any adjustment as written in Eq ??, one should only expect noise and not a coherent beam. This is because we have assumed the wavefront's differential time-of-arrival across the array is the same time delay seen by the correlator. In fact each signal is further delayed by multiple steps in the signal chain. Digital phases in the electronics can be added by the LNAs and FLAs, and coaxial cables, whose lengths vary by up to a meter, can rotate the signal by multiple radians. Therefore in order to coherently sum across the array and beamform, the instrumental phases must be removed. If e_n is the true electric field on the sky as seen by each feed, then the thing we measure is the on-sky signal altered by an effective gain, g_n , and a noise term, n_n .

$$x_n = g_n e_n + n_n \quad (1.11)$$

We have lumped several terms into $g_n = |g_n|e^{i\phi_{g_n}}$, which is composed of a pointing-dependent beam term and any complex gain introduced once light hits the cylinder. Since we really only care about the phase, we can decompose $\arg(g_n)$ as,

$$\phi_{g_n} = \phi_{\text{beam}} + \phi_{\text{an}} + \phi_{\text{e}} + \phi_{\text{fpga}} \quad (1.12)$$

where ϕ_{beam} is the beam's phase for a given pointing, ϕ_{an} comes from the analogue chain (dual-pol feed, coax, etc.), ϕ_{e} is any phase introduced in the electronics, and ϕ_{fpga} are phases applied in the F -engine.

Since the instrumental phases are effectively random, the simplest way to remove them is to solve for them empirically, usually from a point-source on the sky. Using the visibility definition in Eq ??, one can evaluate that all-sky integral assuming the sky's

electric field is produced by a single point-source. This is tantamount to a delta function at a single direction on the sky.

$$V_{m,n}^{\text{ps}} = \int d^2\hat{\mathbf{k}} g_m(\hat{\mathbf{k}}) g_n^*(\hat{\mathbf{k}}) e_m(\hat{\mathbf{k}}) e_n^*(\hat{\mathbf{k}}) \delta(\hat{\mathbf{k}} - \hat{\mathbf{k}}_{\text{ps}}) \quad (1.13)$$

$$= g_m(\hat{\mathbf{k}}_{\text{ps}}) g_n^*(\hat{\mathbf{k}}_{\text{ps}}) e_m(\hat{\mathbf{k}}_{\text{ps}}) e_n^*(\hat{\mathbf{k}}_{\text{ps}}) \quad (1.14)$$

In this equation $\hat{\mathbf{k}}_{\text{ps}}$ is the only direction on the sky with a source — an approximation whose validity we will discuss below — and δ is a Kronecker delta function.

$$V_{m,n}^{\text{ps}} = \quad (1.15)$$

$$V_{m,n} = \int d^2\hat{\mathbf{k}} g_m(\hat{\mathbf{k}}) g_n^*(\hat{\mathbf{k}}) e_m(\hat{\mathbf{k}}) e_n^*(\hat{\mathbf{k}}) \quad (1.16)$$

If we explicitly write the phase information of the sky’s electric field, we can use

$$e_m(\hat{\mathbf{k}}) e_n^*(\hat{\mathbf{k}}) = T(\hat{\mathbf{k}}) e^{2\pi i \hat{\mathbf{k}} \cdot \mathbf{d}_{mn}}. \quad (1.17)$$

$$V_{m,n} = \int d^2\hat{\mathbf{k}} g_m(\hat{\mathbf{k}}) g_n^*(\hat{\mathbf{k}}) T(\hat{\mathbf{k}}) e^{2\pi i \hat{\mathbf{k}} \cdot \mathbf{d}_{mn}} \quad (1.18)$$

Therefore a single correlation can be written as an intensity multiplied by a phase factor that is determined by the source direction’s projection onto that correlation’s baseline. Since that phase factor is calculable via Eq. ??, it can be removed in a process called “fringestopping”. The data can be inspected visually quite easily, since a transiting point-source will fringe as a function of time at a rate corresponding to the projected baseline length, but should not after fringestopping is applied. This is demonstrated with an inter-cylinder Cygnus A transit in Fig. ??.

The $N(N+1)/2$ visibilities we measure can be thought of as the upper triangle of an $N \times N$ complex Hermitian matrix, \mathbf{V} . This is simply the outer product of the signal vector, \mathbf{x} , with its Hermitian conjugate.

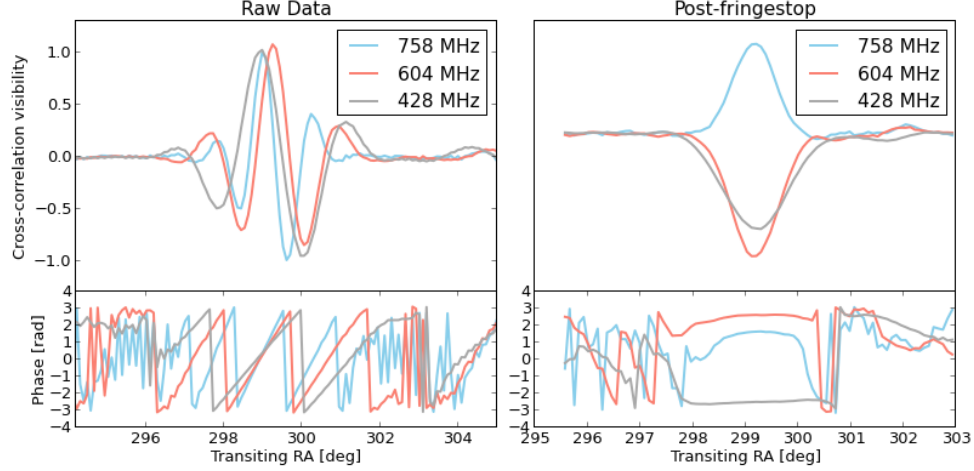


Figure 1.2: An example of the fringing process that is necessary for gain calibration off of a transiting point-source. Since the phase of a visibility will have a time- and frequency-dependent component, the measured correlation will fringe as the earth rotates in a chromatic way. This effect can be removed by multiplying each visibility by $e^{-i\phi_{mn}(t,\nu)}$, as determined by Eq. ?? . The top left panel shows the raw correlation as a function of transiting RA between feeds 1 and 129, which are of the same polarization but on opposite cylinders, separated by 21 m. We plot three different frequencies. The panel below the top left shows the same complex visibility's phase. The slope, or fringe-rate, decreases at lower frequencies, as expected. The right panel show the same data after running it through the fringingstopping pipeline. Though the resulting phases are near flat, implying that the baseline is no long fringeing, the visibilities are not purely real; this is because there are residual instrumental phases. These phases can be solved for using an eigendecomposition now that the array is phased up to a single point-source.

$$\mathbf{V} = \mathbf{xx}^\dagger \approx \begin{pmatrix} |g_0|^2 e_0^2 & \dots & & \\ & g_n g_m^* e_n e_m^* & & \\ & & \ddots & \\ & & & |g_N|^2 e_N^2 \end{pmatrix} \quad (1.19)$$

If the sky is composed of a single point-source then this matrix will be rank one, i.e. there is only one non-zero eigenvalue. One can see this by referring to Eq. ?? and noting

that if the data has been fringestopped, then the sky temperature can be factored out of Eq. ??, which becomes

$$\mathbf{V} = T(\hat{\mathbf{k}}) \mathbf{g} \mathbf{g}^\dagger. \quad (1.20)$$

Therefore by diagonalizing the correlation matrix \mathbf{V} we get a complex eigenvector corresponding to the largest eigenvalue, and that eigenvector is proportional to the gain vector \mathbf{g} . The phase of this eigenvector will be an estimate for the instrumental phases, ϕ_{g_n} , up to some unknown global offset. The goodness of this calibration depends on the validity of our assumption that the correlation matrix is rank one. We can estimate the error on the calibration solution as the ratio of the second largest eigenvalue, λ_2 , to the largest, λ_1 . For typical frequencies we get values of $\frac{\lambda_2}{\lambda_1} \sim 3\%$.

These algorithms have been implemented in a pre-beamforming pipeline written in `Python`. Each day a point-source transit is fringestopped and a calibration solution is solved for. The source chosen depends on the solar time of its transit: Since the sun is extraordinarily bright in our band it will always appear in the sidelobes, so the transit has to be at night for good calibration solutions. Historically, we have used Cygnus A in the spring and summer, Cassiopeia A in the summer and fall, and Tau A in the winter. Whatever we calibrate off of, the phases of that solution are written to pickle files that are readable by the Pathfinder’s FPGAs. The FPGA then applies complex gains after channelization, which in theory should provide the beamforming kernel with voltages whose phases are purely geometric.

1.5 FRB VLBI search

In 1967 Canada achieved an historic feat by doing the first ever successful VLBI observation. The fringes were obtained between DRAO and ARO, with a baseline of 3,074 km (?). This result was given a “Milestone” award from The Institute of Electrical and Electronics Engineers (IEEE), which was also awarded for the inception of the Internet, transmission of transatlantic radio signals, and the discovery of Maxwell’s equations (?). We have attempted to recreate the same VLBI baseline, but instead of using the considerable spatial resolution on quasars as in 1967, we are attempting to localize FRBs.

1.5.1 Motivation

The CHIME Pathfinder is meant to have only one synthetic beam. Its purpose is primarily to act as a test-bed for the more powerful pulsar and FRB backends that will

be attached to the full four-cylinder CHIME. However since the Pathfinder is on sky at all times and the beamformer we have built does not interrupt the ongoing cosmology acquisition, we decided to build a preliminary FRB search. We also have as many as three other telescopes onto which we can mount CHIME feeds and observe in our band: the Algonquin Radio Observatory (ARO), the John A. Galt 26m, and the GreenBank 140ft telescope. This would allow for the first ever VLBI detection of an FRB.

This is interesting for a few reasons. From a development standpoint it allows us to understand better various stages of the CHIME-FRB pipeline, including the rate of RFI false-positives, our algorithm’s search efficiency, and specs on the regularity and precision of instrumental gain removal. It will also give us a good sense of how the real CHIME beams behave on the sky. Perhaps most interestingly, we could reasonably expect to see a burst after several months of observing, hopefully in coincidence with the telescopes previously mentioned. We could therefore not only detect an FRB with sub-arcsecond resolution, but also would the first source in our band, at 400-800 MHz, including full polarization information. While searching for fast radio bursts, we could also find RRATs and new slow pulsars, since a significant fraction of the Galaxy transits each day.

1.5.2 Implementation

We have had a working beamforming backend on the CHIME Pathfinder since October 2015. It has been used primarily for short tracking pulsar observations, but had stability issues on timescales of \sim days, meaning we could not run it for long periods without interfering with the regular cosmology acquisition. However in the past several months a number of new features were added that allow not only long-term beamforming captures, but also transient searching.

A real-time, multithreaded acquisition code that takes in the VDIF packets coming out of the X-engine, and rearranges them to either be written to disk or search for FRBs¹. Attached to this packet reader was a tree-dedispersion search code, some of which had been used before on GreenBank 100m data and a real-time ARO search². The CHIME acquisition software `kotekan` was altered in a number of ways, fixing the long-term stability issues in the beamforming kernel. These systems were synthesized into a real-time transient search backend that has been on sky since May 2016. It is outlined in Fig. ?? on page ??.

Since CHIME is a transit telescope with a long north-south beam, our formed beam is effectively confined to the meridian. This means we must choose an optimal declination

¹https://github.com/kmsmith137/ch_vdif_assembler

²https://github.com/kiyo-masui/burst_search

on which to park the beam. As a sanity check, we spent ~ 10 days pointed at the declination of pulsar B0329+54, which is the brightest switching source in the northern sky in our band. It is dispersed with $26.833 \text{ pc cm}^{-3}$ and its individual pulses are bright enough to detect, meaning our tree-dedispersion algorithm ought to find its individual pulses. During the ten or so minutes that the source is in our beam each day, the algorithm looks at time blocks of 100 seconds, searches for DMs between 10-2000 pc cm^{-3} with widths between 1-100 ms, and looks for peaks above 8σ . If it finds something it “triggers” and writes out an image file containing the peak in DM / arrival time space, a dedispersed waterfall plot, a dedispersed pulse profile, and a fluence frequency spectrum. An example of the B0329+54 is shown in Fig.???. It also writes `numpy` arrays containing the squared and summed intensity data. It then moves on to the next block of 100 seconds, overlapping with the previous one by 18 seconds.

1.5.3 Results

As we discuss in chapter ??, there is a large uncertainty in the FRB rate between 400-800 MHz. There is even greater uncertainty in the expected rate for a telescope like the CHIME Pathfinder. This is because at this time all FRBs have been detected with large-collecting area, highly sensitive single-dish telescopes (GBT, Parkes, and Arecibo). Therefore in order to extrapolate the rate estimates on to the Pathfinder, which does not have much collecting area and whose beam is quite large, one needs to know the underlying flux distribution. As we will show in Eq. ??, the rate depends on the product of the telescope’s field-of-view (FoV) and a thermal sensitivity term. This scales $\propto A^{-1}A^\gamma$, where A is collecting area and γ is the FRB flux distribution’s power-law index, which is $3/2$ if FRBs are non-cosmological and Euclidean. If $\gamma < 1$, as is expected in the cosmological FRB scenario, then small telescopes are actually advantageous over large single-pixel telescopes since the beamsizes become more important.

With a dish like the Pathfinder the rate is roughly 10 times higher if $\gamma \approx 0.8$ (cosmological scenario) compared to the Euclidean scenario. This is because its relatively low sensitivity per steradian requires there be large numbers of very bright bursts, which one gets from a flat distribution.

1.6 Conclusion

Acknowledgements

We thank Andre Recnik

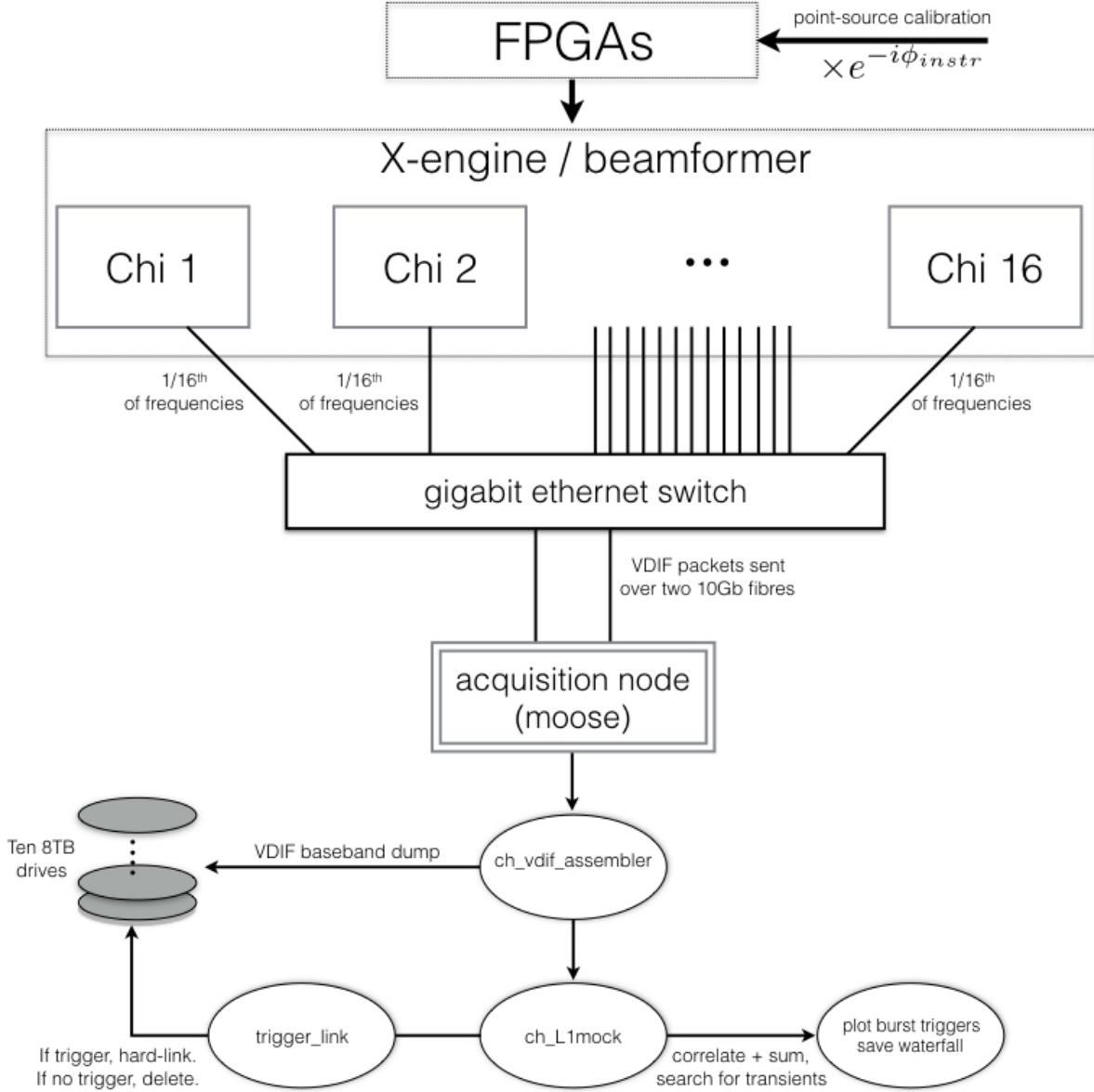


Figure 1.3: Block diagram of the beamforming backend on CHIME Pathfinder. A calibration solution is obtained from a bright point-source transit, the phases of which are fed into the FPGAs where they are applied as a digital gain. All antenna signals are then sent the *X*-engine, comprised of 16 GPU nodes. Each node applies geometric phases then sums the voltage stream across all antennas with the same polarization. The two resultant beams are then sent to our acquisition machine *moose* as VDIF packets, where a multi-threaded capture code, *ch_vdif_assembler*. At this point the baseband data are either written to disk as scrambled baseband VDIF, or they are reorganized in time and frequency. The ordered data are searched for FRBs after squaring and integrating to \sim millisecond cadence using a tree-dedispersion algorithm. If there is a trigger, then the corresponding baseband data is hard-linked. Old files that haven't been hard-linked are deleted periodically.

Bibliography

- Bandura, K. e. a. 2014, in Society of Photo-Optical Instrumentation Engineers (SPIE) Conference Series, Vol. 9145, Society of Photo-Optical Instrumentation Engineers (SPIE) Conference Series, 22
- Barrau, A., Rovelli, C., & Vidotto, F. 2014, Phys. Rev. D, 90, 127503
- Becker, W., Kramer, M., Jessner, A., et al. 2006, ApJ, 645, 1421
- Bower, G. C., Deller, A., Demorest, P., et al. 2014, ApJ, 780, L2
- Burke, B. F., & Graham-Smith, F. 2014, An Introduction to Radio Astronomy
- Connor, L., Sievers, J., & Pen, U.-L. 2016, MNRAS, 458, L19
- Cordes, J. M., Bhat, N. D. R., Hankins, T. H., McLaughlin, M. A., & Kern, J. 2004, ApJ, 612, 375
- Cordes, J. M., & Wasserman, I. 2015, ArXiv e-prints 1501.00753, arXiv:1501.00753
- Dennett-Thorpe, J., & de Bruyn, A. G. 2002, Nature, 415, 57
- Falcke, H., & Rezzolla, L. 2014, A&A, 562, A137
- Hippke, M., Domainko, W. F., & Learned, J. G. 2015, ArXiv e-prints 1503.05245, arXiv:1503.05245
- Kashiyama, K., Ioka, K., & Mészáros, P. 2013, ApJ, 776, L39
- Katz, J. I. 2015, ArXiv e-prints 1505.06220, arXiv:1505.06220
- Kulkarni, S. R., Ofek, E. O., Neill, J. D., Zheng, Z., & Juric, M. 2014, ApJ, 797, 70
- Loeb, A., Shvartzvald, Y., & Maoz, D. 2014, MNRAS, 439, L46

- Lorimer, D. R., Bailes, M., McLaughlin, M. A., Narkevic, D. J., & Crawford, F. 2007, *Science*, 318, 777
- Luan, J., & Goldreich, P. 2014, *ApJ*, 785, L26
- Lyubarsky, Y. 2014, *MNRAS*, 442, L9
- Maoz, D., Loeb, A., Shvartzvald, Y., et al. 2015, *ArXiv e-prints* 1507.01002, arXiv:1507.01002
- Masui, K., Lin, H.-H., Sievers, J., et al. 2015, *ArXiv e-prints*, arXiv:1512.00529
- McQuinn, M. 2014, *ApJ*, 780, L33
- Mickaliger, M. B., McLaughlin, M. A., Lorimer, D. R., et al. 2012, *ApJ*, 760, 64
- Narayan, R. 1992, *Royal Society of London Philosophical Transactions Series A*, 341, 151
- Oppermann, N., Junklewitz, H., Greiner, M., et al. 2015, *A&A*, 575, A118
- Pen, U.-L., & Connor, L. 2015, *ArXiv e-prints* 1501.01341, arXiv:1501.01341
- Pen, U.-L., & Levin, Y. 2014, *MNRAS*, 442, 3338
- Petroff, E., Bailes, M., Barr, E. D., et al. 2015, *MNRAS*, 447, 246
- Popov, S. B., & Postnov, K. A. 2007, *ArXiv e-prints*, arXiv:0710.2006
- Potter, T. M., Staveley-Smith, L., Reville, B., et al. 2014, *ApJ*, 794, 174
- Rane, A., Lorimer, D. R., Bates, S. D., et al. 2015, *ArXiv e-prints* 1505.00834, arXiv:1505.00834
- Rankin, J. M., Campbell, D. B., Isaacman, R. B., & Payne, R. R. 1988, *A&A*, 202, 166
- Sallmen, S., Backer, D. C., Hankins, T. H., Moffett, D., & Lundgren, S. 1999, *ApJ*, 517, 460
- Taylor, M., Cinabro, D., Dilday, B., et al. 2014, *ApJ*, 792, 135
- Thompson, A. R., Moran, J. M., & Swenson, G. W. 1986, *Interferometry and synthesis in radio astronomy*
- Thornton, D., Stappers, B., Bailes, M., et al. 2013, *Science*, 341, 53

Totani, T. 2013, PASJ, 65, L12

Xu, J., & Han, J. L. 2015, ArXiv e-prints 1504.00200, arXiv:1504.00200

Zanardo et al. 2014, ApJ, 796, 82